















Testing the Rossby Paradigm: Weakened Magnetic Braking in early K-type Stars

TRAVIS S. METCALFE ¹, PASCAL PETIT ², JENNIFER L. VAN SADERS ³, THOMAS R. AYRES ⁴, DEREK BUZASI ⁵,
OLEG KOCHUKHOV ⁶, KEIVAN G. STASSUN ⁷, MARC H. PINSONNEAULT ⁸, ILYA V. ILYIN ⁹, KLAUS G. STRASSMEIER ⁹,
ADAM J. FINLEY ¹⁰, RAFAEL A. GARCÍA ¹⁰, YUXI (LUCY) LU ⁸, AND VICTOR SEE ¹¹

¹Center for Solar-Stellar Connections, White Dwarf Research Corporation, 9020 Brumm Trail, Golden, CO 80403, USA

²Université de Toulouse, CNRS, CNES, 14 avenue Edouard Belin, 31400, Toulouse, France

³Institute for Astronomy, University of Hawai‘i, 2680 Woodlawn Drive, Honolulu, HI 96822, USA

⁴Center for Astrophysics and Space Astronomy, 389 UCB, University of Colorado, Boulder, CO 80309, USA

⁵Department of Astronomy & Astrophysics, University of Chicago, Chicago, IL 60637, USA

⁶Department of Physics and Astronomy, Uppsala University, Box 516, SE-75120 Uppsala, Sweden

⁷Vanderbilt University, Department of Physics & Astronomy, 6301 Stevenson Center Lane, Nashville, TN 37235, USA

⁸Department of Astronomy, The Ohio State University, 140 West 18th Avenue, Columbus, OH 43210, USA

⁹Leibniz-Institut für Astrophysik Potsdam (AIP), An der Sternwarte 16, D-14482 Potsdam, Germany

¹⁰Université Paris-Saclay, Université Paris Cité, CEA, CNRS, AIM, 91191, Gif-sur-Yvette, France

¹¹School of Physics & Astronomy, University of Birmingham, Edgbaston, Birmingham B15 2TT, UK

ABSTRACT

There is an intricate relationship between the organization of large-scale magnetic fields by a stellar dynamo and the rate of angular momentum loss due to magnetized stellar winds. An essential ingredient for the operation of a large-scale dynamo is the Coriolis force, which imprints organizing flows on the global convective patterns and inhibits the complete cancellation of bipolar magnetic regions. Consequently, it is natural to expect a rotational threshold for large-scale dynamo action and for the efficient angular momentum loss that it mediates through magnetic braking. Here we present new observational constraints on magnetic braking for an evolutionary sequence of six early K-type stars. To determine the wind braking torque for each of our targets, we combine spectropolarimetric constraints on the large-scale magnetic field, Ly α or X-ray constraints on the mass-loss rate, as well as uniform estimates of the stellar rotation period, mass, and radius. As identified previously from similar observations of hotter stars, we find that the wind braking torque decreases abruptly by more than an order of magnitude at a critical value of the stellar Rossby number. Given that all of the stars in our sample exhibit clear activity cycles, we suggest that weakened magnetic braking may coincide with the operation of a subcritical stellar dynamo.

Keywords: Spectropolarimetry; Stellar evolution; Stellar magnetic fields; Stellar rotation; Stellar winds

1. INTRODUCTION

Recent observations and numerical simulations suggest that magnetic stellar evolution is substantially more complex than has previously been assumed. The global stellar dynamo is responsible for the production and large-scale organization of magnetic fields, but the dominant scale of the magnetic morphology may change on stellar evolutionary timescales (Buzasi 1997; Garraffo et al. 2016, 2018). It has been suggested that the dynamo might shift from a mode that weakly couples to the stellar wind in the saturated regime to a mode that strongly couples to it in the unsaturated regime (Brown 2014). Subsequently, the dipole-dominated fields strongly couple the evolution of rotation and magnetism through angular momentum loss driven by magnetized stellar winds, a

process known as magnetic braking (Weber & Davis 1967; Skumanich 1972; Kawaler 1988). When rotation eventually becomes too slow to imprint substantial Coriolis forces onto the global convective patterns, organizing flows such as differential rotation and meridional circulation may become weakened and the field might lose its large-scale organization, leading to a more complex morphology and decoupling the continued evolution of rotation and magnetism. These transitions appear to be accompanied by corresponding changes in magnetic variability—from multiperiodic or stochastic, to well-ordered periodic cycling, to constant or flat activity (Metcalf & van Saders 2017; Brun et al. 2022).

The evidence for weakened magnetic braking (WMB) in old solar-type stars has expanded and solidified since it was

initially suggested to explain anomalously rapid rotation in old field stars observed by the Kepler mission (van Saders et al. 2016). The original sample included only 21 stars with asteroseismic ages (Metcalf et al. 2014) and rotation periods determined from spot modulations (García et al. 2014). However, the imprint of WMB was also evident in the distribution of 34,000 rotation periods in the Kepler field (McQuillan et al. 2014). Subsequent forward modeling of this sample suggested that standard spin-down models could not reproduce the observed long-period edge (van Saders et al. 2019), and more precise effective temperatures revealed a mixed population along the edge with diverse ages spanning the second half of main-sequence lifetimes (David et al. 2022). The asteroseismic sample was also expanded, with rotation periods determined from mode splitting rather than spot modulation (Hall et al. 2021), and the paucity of old slow rotators was confirmed with $v \sin i$ measurements (Masuda 2022).

Modeling this phenomenon is complex because stellar dynamos are not simple functions of global stellar properties. Historically it was difficult to measure stellar magnetic fields directly, and investigators used stellar activity diagnostics as proxies for field strength. In a landmark paper, Noyes et al. (1984) demonstrated that activity indicators scaled with the ratio of the rotation period to the convective overturn timescale, or Rossby number ($Ro \equiv P_{\text{rot}}/\tau_c$), across a wide range of stellar rotation periods and masses. Recent work has confirmed that this scaling appears to hold for starspot filling factor (Cao & Pinsonneault 2022) and Zeeman broadening measurements (Reiners et al. 2022). It is therefore reasonable to hypothesize that the disruption of the dynamo might also scale with Ro , and that the onset of WMB might be identified with a critical Rossby number (Ro_{crit}). Updated asteroseismic modeling and hierarchical Bayesian analysis has recently established a precise estimate of Ro_{crit} for the onset of WMB (Saunders et al. 2024).

More direct observational constraints on magnetic braking have gradually become available over the past several years for a small sample of bright main-sequence stars. Spectropolarimetric snapshots of the late F-type stars 88 Leo and ρ CrB suggested a substantial shift in magnetic morphology across Ro_{crit} (Metcalf et al. 2019) accompanied by a large change in the estimated wind braking torque (Metcalf et al. 2021). An evolutionary sequence of solar analogs provided additional constraints from archival Zeeman-Doppler Imaging (ZDI) maps of HD 76151 and 18 Sco along with new high signal-to-noise (S/N) snapshots of 16 Cyg A and 16 Cyg B (Metcalf et al. 2022), reinforcing the conclusions drawn from the hotter stars. The extension of this approach to the late G-type stars 61 UMa and τ Cet (Metcalf et al. 2023a) suggested that the wind braking torque must decrease dramatically at the same value of Ro_{crit} determined from indirect constraints (cf. Metcalf et al. 2024b; Saunders et al. 2024).

In this paper, we provide new constraints on magnetic braking for an evolutionary sequence of six early K-type stars (ϵ Eri, σ Dra, 107 Psc, HD 103095, HD 219134, HD 166620) from the analysis of two published and two unpublished ZDI maps, as well as two recent high S/N snapshots from the Large Binocular Telescope (LBT). Based on the Rossby paradigm, these stars should exhibit a change in dynamo behavior at longer rotation periods than their F- and G-type counterparts. In Section 2 we describe the observations that were used to estimate the wind braking torque, including spectropolarimetry to infer the large-scale magnetic field strength and morphology (§2.1), archival Ly α and X-ray observations to estimate the mass-loss rate (§2.2), and analysis of the broadband spectral energy distribution (SED) to estimate the stellar radius and mass (§2.3). In Section 3 we combine these inputs with stellar rotation periods adopted from the literature to match the observed stellar properties with rotational evolution models that include WMB (§3.1) and to estimate the wind braking torque for each of our targets (§3.2). Finally, in Section 4 we summarize and discuss our results, concluding that WMB may coincide with the operation of a subcritical stellar dynamo.

2. OBSERVATIONS

2.1. Spectropolarimetry

To constrain the strength and morphology of the large-scale magnetic field in each of our targets, we relied on new LBT snapshot observations of HD 103095 and HD 166620 (§2.1.1), we constructed new ZDI maps from archival measurements of σ Dra (§2.1.2) and 107 Psc (§2.1.3), and we adopted the results from previously published ZDI maps for ϵ Eri (Jeffers et al. 2014) and HD 219134 (Folsom et al. 2018a). We selected the 2008 map for ϵ Eri, which samples the mean activity level (as does the 2016 map of HD 219134). For the wind braking calculations, we made the conservative assumption that the snapshot Stokes V profiles can be attributed entirely to an axisymmetric dipole field, which maximizes the resulting torque estimate. For the new and previously published ZDI maps, we followed the procedures described in Metcalf et al. (2022) to convert the total magnetic flux in a given spherical harmonic degree (B_ℓ) into equivalent polar field strengths for the dipole, quadrupole, and octupole components (B_d, B_q, B_o), which are the required inputs for the wind braking prescription of Finley & Matt (2018).

2.1.1. LBT Snapshot Observations

We acquired circular polarization (Stokes V) observations of HD 103095 and HD 166620 on the nights of 2023 December 6 and 2024 July 5, respectively, using the Potsdam Echelle Polarimetric and Spectroscopic Instrument (PEPSI; Strassmeier et al. 2015) at the 2×8.4 m LBT. The instrument was configured for a resolving power of $R = 130,000$

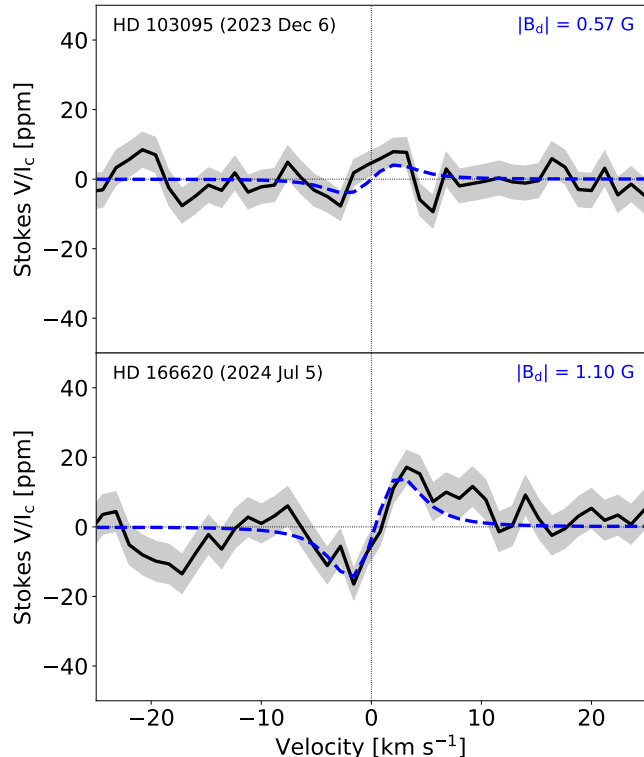


Figure 1. Stokes V polarization profiles for HD 103095 (top) and HD 166620 (bottom) from LBT observations on 2023 December 6 and 2024 July 5, respectively. The mean LSD profile is shown as a black line with uncertainties indicated by the gray shaded area. The dashed blue line is an axisymmetric model profile assuming dipole morphology with a fixed inclination.

and covered the wavelength intervals 475–540 nm and 623–743 nm. The observational data were reduced as described in Metcalfe et al. (2019). Anticipating the extremely weak polarization signals for these two stars, we adopted exposure times of 7200–8640 s, resulting in a peak S/N \sim 3300–4400 per pixel in the extracted spectra.

The least-squares deconvolution (LSD; Kochukhov et al. 2010) technique was utilized to boost the S/N further by combining the profiles of all suitable metal lines. We constructed masks comprising 1630–2420 lines deeper than a few per cent of the continuum with the help of the VALD database (Ryabchikova et al. 2015), based on the spectroscopic parameters from Valenti & Fischer (2005) for HD 103095 and Brewer et al. (2016) for HD 166620. The LSD analysis yielded mean Stokes V profiles characterized by a polarimetric precision of about 5 ppm (see Figure 1). This yielded a secure detection of the Zeeman polarization signature in HD 166620, with a mean longitudinal magnetic field $\langle B_z \rangle = -0.28 \pm 0.07$ G (where the sign indicates the dominant field polarity). For HD 103095 there was no significant detection, and the mean longitudinal field was consistent with zero, $\langle B_z \rangle = 0.00 \pm 0.11$ G.

We applied the Stokes V profile modeling technique described in Metcalfe et al. (2019) to constrain the strength of the global magnetic field by assuming an axisymmetric dipole morphology. We fixed the inclination of the stellar rotation axis using the analytic expressions from Bowler et al. (2023) to calculate posteriors given the measurements of $v \sin i$, rotation period, and radius. The posterior distribution peaked at $i = 51^\circ$ for HD 103095, yielding a best-fit dipole field strength of $B_d = -0.57$, and $i = 37^\circ$ for HD 166620, yielding $B_d = -1.10$ G. The predicted circular polarization profiles are illustrated with dashed blue lines in Figure 1.

2.1.2. ZDI of σ Dra

Multiple spectropolarimetric observations of σ Dra are available on the PolarBase archive (Petit et al. 2014). All of them were collected with the NARVAL spectropolarimeter (Aurière 2003), offering a simultaneous recording of the full spectral domain between 370 nm and 1000 nm except a few, small wavelength intervals in the reddest part of the spectra. Following the standard data reduction performed with the LIBRESPLIT automated package (Donati et al. 1997), all observations were processed with the LSD multi-line method from which we extracted, for every spectrum, a single pseudo-line profile with greatly increased S/N. This standard approach (Donati et al. 1997; Kochukhov et al. 2010) is a necessary step in the search for weak stellar magnetic fields, which generally produce polarized Zeeman signatures well below the noise level in individual lines. Thanks to the large spectral span of NARVAL, more than 5000 photospheric spectral lines were used together, with a line list provided by the VALD database (Ryabchikova et al. 2015), for an effective temperature and surface gravity close to those of σ Dra, keeping only lines deeper than 40% of the continuum level, and skipping wavelength intervals plagued by telluric bands or blended with broad chromospheric lines. The pseudo-line profiles have a normalized wavelength of 650 nm and a normalized Landé factor close to 1.2. For our dataset, the outcome of this procedure was the successful detection of Zeeman signatures in circular polarization (Stokes V) for most of the available observations (as illustrated in Figure 2), thanks to a final S/N close to 40,000.

Observations of σ Dra were gathered over three distinct epochs in 2007, 2009, and 2019. The dataset obtained in 2009 is the only one with a sampling of the stellar rotation sufficient for tomographic inversion. Our magnetic mapping was, therefore, focused on this specific time series. A quick analysis of the remaining data (not shown here) reveals that in 2007 the field polarity was always negative whenever a signature was detected (3 detected magnetic signatures, among 4 observations spanning 12 days). In 2009, over a campaign spanning 13 days, 6 visits showed a positive polarity, one displayed a negative polarity, and one visit did not lead to a

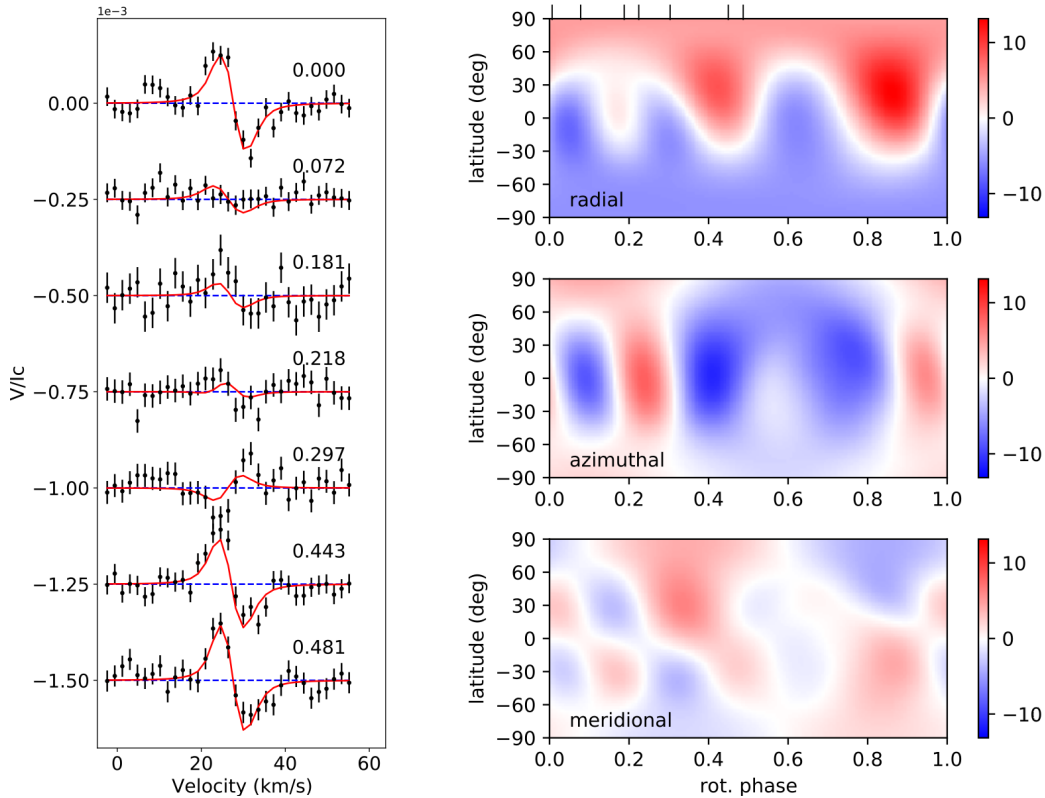


Figure 2. Left: Stokes V LSD profiles obtained from NARVAL observations of σ Dra. Observations are shown as black dots (along with their error bars), while the ZDI model is displayed with red lines. Blue dashes show the null level, and the rotational phases of the observations are labeled on the right side of the plot. Successive observations are vertically shifted for clarity. Right: ZDI magnetic map of σ Dra in equirectangular projection. Each panel shows one component of the magnetic vector in spherical coordinates. The field strength is color-coded and expressed in Gauss. The rotation phases of observation are shown with vertical ticks above the top panel.

detection. In 2019, 3 observations spanning 19 days consistently showed a negative polarity. The consistency of field polarities observed at each epoch, considered with the successive sign switches between epochs, may be indicative of a solar-like cycle taking place in σ Dra, with regular polarity flips of the global magnetic field (e.g., Boro Saikia et al. 2018; do Nascimento et al. 2023). Indeed, the time series of chromospheric activity measurements presented in Baum et al. (2022) show that σ Dra has a 6.2 year activity cycle which was maximum in 2009 and near a magnetic minimum in 2007 and 2019, consistent with the observed polarity flips.

We used the series of 7 observations collected in 2009, between June 23 and July 6, to model the large-scale magnetic geometry of σ Dra using the ZDI method (Semel 1989). We employed the Python code developed by Folsom et al. (2018b,a), following the algorithm described by Donati et al. (2006). We reproduced the procedure of Petit et al. (2021) to model the time series of LSD pseudo-line profiles, assuming that the observed variability of polarized signatures is induced entirely by rotational modulation. The ephemeris adopted to compute rotational phases was set as $HJD_{\text{obs}} = HJD_0 + P_{\text{rot}} \times \Phi$ where Φ is the rotational phase, HJD_{obs} is the heliocentric Julian date of observation, HJD_0 is a reference

date that we set to 2455005.61704, and P_{rot} is the rotation period, set to 27 d (Baliunas et al. 1996). The phase coverage obtained here presents a relatively dense sampling of phases between 0.0 and 0.5 but with a gap for the other half of the rotation period. Other standard input parameters of ZDI include a projected rotational velocity $v \sin i = 1.4 \text{ km s}^{-1}$ (Brewer et al. 2016), an angle between the spin axis and the line of sight set to 60° , and a radial velocity equal to 26.55 km s^{-1} . Differential rotation was not included in the model because it cannot be reliably constrained with the available phase coverage. The spherical harmonic expansion of the magnetic field was limited to $\ell_{\text{max}} = 10$ because no improvement of the fit was observed when a more complex field was allowed. A unit χ^2 was obtained for the best model, showing that the assumptions listed above enabled us to produce a model fitting the data within their error bars. The outcome of the fit is illustrated with red lines in the left panel of Figure 2, with the ZDI map shown in the right panel.

The magnetic geometry features a mean field strength of 7 G and a peak strength of 15 G. A majority of the magnetic energy (82%) is reconstructed in the poloidal component. An inclined dipole stores about 45% of the poloidal magnetic energy, with a polar strength of 7 G. The field configuration

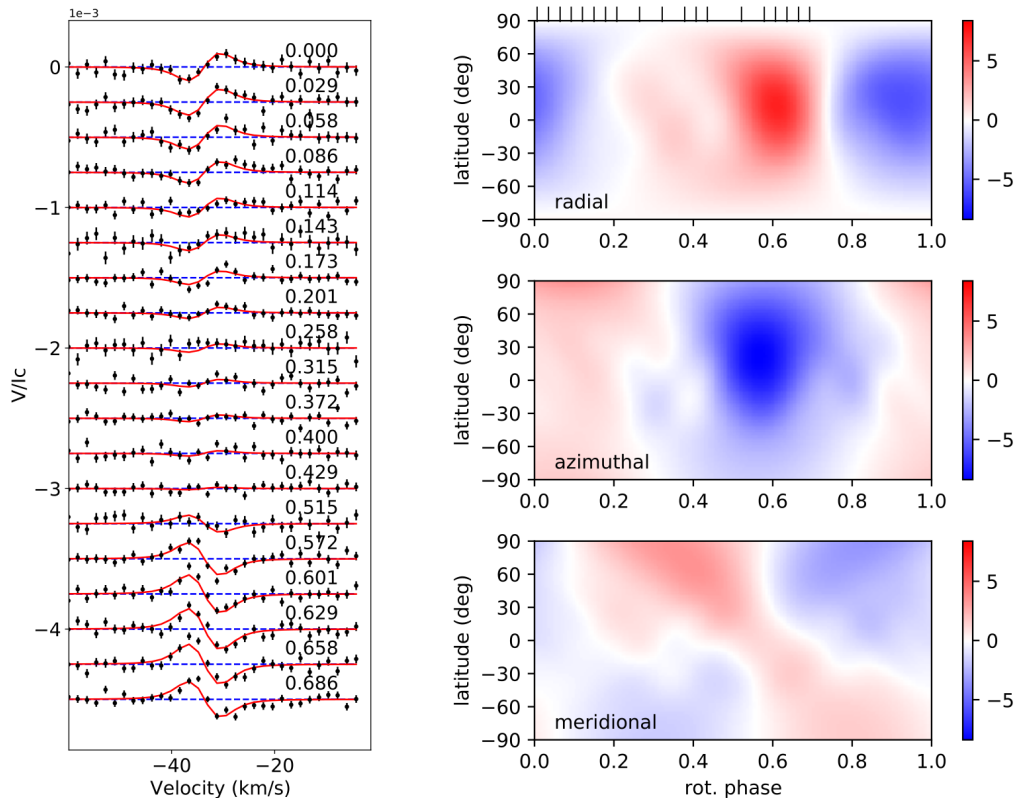


Figure 3. Left: Stokes V LSD profiles obtained from NARVAL observations of 107 Psc. Observations are shown as black dots (along with their error bars), while the ZDI model is displayed with red lines. Blue dashes show the null level, and the rotational phases of the observations are labeled on the right side of the plot. Successive observations are vertically shifted for clarity. Right: ZDI magnetic map of 107 Psc in equirectangular projection. Each panel shows one component of the magnetic vector in spherical coordinates. The field strength is color-coded and expressed in Gauss. The rotation phases of observation are shown with vertical ticks above the top panel.

is mostly non-axisymmetric, with only 35% of the magnetic energy in $m = 0$ spherical harmonic modes.

2.1.3. ZDI of 107 Psc

The spectropolarimetric dataset modeled for 107 Psc was obtained in 2008, with 19 visits between January 22 and February 15 using the NARVAL spectropolarimeter. Two other observing epochs are available on the PolarBase archive—one from early 2007, and a second from the summer of 2007. We did not focus on these earlier datasets, because they displayed a sparser phase coverage (early 2007) or suffered from a lower detection rate (mid-2007). The procedures applied to extract Zeeman signatures and to model the magnetic geometry follow the same steps as those described above for σ Dra.

The set of Stokes V LSD signatures obtained in 2008 are shown in Figure 3. They display a negative polarity until January 29. After this date, the signatures fade away until February 9, when a positive polarity progressively grows. Unfortunately, the time span available for this run was limited to 24 days, preventing us from observing about 30% of the complete rotation to recover the negative polarity. The simple observation of an alternation of polarities tells us, be-

fore any tomographic modeling, that the magnetic geometry at this epoch was very non-axisymmetric. We note that the observations in 2007 are mostly consistent with this picture, with both polarities successively observed in early 2007 and an amplitude compatible with 2008 values, while the few detections obtained during the summer display a positive polarity, again of a roughly similar amplitude.

The ZDI map was computed assuming a rotation period of 35 d, $v \sin i = 0.1 \text{ km s}^{-1}$ (Brewer et al. 2016), a mean radial velocity of -33.7 km s^{-1} , and a spin axis inclination of 60° . The reference rotational phase was set to Julian date $HJD_0 = 2454488.28715$. As for σ Dra, the level of detail in the Stokes V data did not require a spherical harmonic expansion above $\ell_{\max} = 10$. This set of parameters allowed the ZDI inversion to reach a reduced χ^2 of 0.98. The result of the fit is shown with the Stokes V profiles in the left panel of Figure 3, with the ZDI map shown in the right panel.

The magnetic geometry features an average field strength of 4 G. A majority (84%) of the magnetic energy is reconstructed in the poloidal component, and a very tilted dipole accounts for slightly more than 80% of the poloidal magnetic energy. As expected, the field configuration is very non-axisymmetric, with only 12% of the magnetic energy in

Table 1. Stellar Properties of the Evolutionary Sequence

	ϵ Eri	σ Dra	107 Psc	HD 103095	HD 219134	HD 166620	Sources
T_{eff} (K)	5146 ± 44	5242 ± 25	5190 ± 25	4950 ± 44	4835 ± 44	4970 ± 25	1, 2
[M/H] (dex)	0.00 ± 0.03	-0.21 ± 0.01	-0.03 ± 0.01	-1.16 ± 0.03	$+0.09 \pm 0.03$	-0.10 ± 0.01	1, 2
$\log g$ (dex)	4.57 ± 0.06	4.56 ± 0.03	4.51 ± 0.03	4.65 ± 0.06	4.56 ± 0.06	4.51 ± 0.03	1, 2
P_{cyc} (yr)	2.95 ± 0.03	6.2 ± 0.1	9.6 ± 0.1	7.30 ± 0.08	11.6 ± 0.3	15.8 ± 0.3	3, 4, 5, 6
$\log \langle R'_{\text{HK}} \rangle$ (dex)	-4.455	-4.832	-4.912	-4.896	-4.890	-4.955	6, 7
P_{rot} (days)	12 ± 0.5	27 ± 0.5	35 ± 0.5	31 ± 0.5	42 ± 0.9	43 ± 0.5	7, 8
Inclination ($^\circ$)	46 ± 2	60	60	51	77 ± 8	37	8, 9, 10
$ B_d $ (G)	14.6	5.68	4.24	0.57 ± 0.03	2.39	$1.10^{+0.42}_{-0.40}$	8, 9, 10
$ B_q $ (G)	8.78	4.82	2.77	...	4.05	...	8, 9, 10
$ B_o $ (G)	5.90	4.76	1.37	...	1.19	...	8, 9, 10
L_X (10^{27} erg s^{-1})	19.1 ± 3.5	$5.1^{+1.9}_{-1.4}$	$1.2^{+0.6}_{-0.4}$	$0.17^{+0.05}_{-0.04}$	0.72 ± 0.05	1.1 ± 0.3	11
Mass-loss rate (\dot{M}_\odot)	30	$3.05^{+1.17}_{-0.79}$	$0.93^{+0.39}_{-0.28}$	$0.30^{+0.10}_{-0.08}$	0.50	$0.92^{+0.22}_{-0.23}$	11, 12
Luminosity (L_\odot)	0.304 ± 0.007	0.402 ± 0.009	0.431 ± 0.010	0.222 ± 0.008	0.257 ± 0.009	0.336 ± 0.008	13
Radius (R_\odot)	0.694 ± 0.014	0.772 ± 0.005	0.813 ± 0.012	0.641 ± 0.017	0.724 ± 0.015	0.782 ± 0.012	13, 14
Mass (M_\odot)	0.86 ± 0.05	0.84 ± 0.01	0.87 ± 0.05	0.60 ± 0.04	0.80 ± 0.05	0.80 ± 0.05	13, 14
Age, astero (Gyr)	...	4.54 ± 0.92	10.2 ± 1.5	...	14, 15
Age, gyro (Gyr)	$1.3^{+0.23}_{-0.20}$	$5.12^{+0.94}_{-0.87}$	$6.88^{+1.19}_{-1.13}$	$7.12^{+1.34}_{-1.21}$	$8.18^{+1.48}_{-1.40}$	$9.16^{+1.47}_{-1.40}$	16
Age, WMB (Gyr)	$1.46^{+0.25}_{-0.22}$	$5.65^{+1.14}_{-0.97}$	$7.72^{+1.80}_{-1.35}$	$8.51^{+2.58}_{-1.77}$	$8.83^{+1.69}_{-1.52}$	$9.5^{+2.15}_{-1.65}$	16
Ro, rotation	0.31 ± 0.02	0.76 ± 0.05	0.90 ± 0.05	0.91 ± 0.06	0.86 ± 0.05	$0.98^{+0.06}_{-0.05}$	16
Ro, activity	0.33 ± 0.01	0.78 ± 0.02	0.93 ± 0.02	0.90 ± 0.02	0.89 ± 0.02	1.03 ± 0.02	17
Torque (10^{30} erg)	$13.9^{+1.8}_{-1.5}$	$1.06^{+0.26}_{-0.20}$	$0.383^{+0.116}_{-0.090}$	$0.019^{+0.007}_{-0.005}$	$0.095^{+0.010}_{-0.009}$	$0.081^{+0.051}_{-0.039}$	17

References—(1) Valenti & Fischer (2005); (2) Brewer et al. (2016); (3) Metcalfe et al. (2013); (4) Baum et al. (2022); (5) Baliunas et al. (1995); (6) Johnson et al. (2016); (7) Baliunas et al. (1996); (8) Folsom et al. (2018a); (9) Jeffers et al. (2014); (10) Section 2.1; (11) Section 2.2; (12) Wood et al. (2021); (13) Section 2.3; (14) Hon et al. (2024); (15) Li et al. (2025); (16) Section 3.1; (17) Section 3.2

$m = 0$ spherical harmonic modes. We note that this same dataset has been used to reconstruct the ZDI map of 107 Psc for two earlier studies (Vidotto et al. 2014; See et al. 2016). The updated model is mostly consistent with the previous version, although the field strength recovered here is slightly larger. This difference is primarily due to modified criteria adopted to ensure that the ZDI code does not overfit or underfit the data (we follow the method employed by Bellotti et al. 2024). Stellar properties are listed in Table 1.

2.2. X-Ray Data

Our target stars have a variety of archival X-ray data, primarily from the venerable 1990s Röntgensatellit (ROSAT), both the all-sky survey (RASS, using the PSPC proportional counter) and post-survey pointings with the PSPC and HRI (micro-channel-based sensor). In some cases, there are contemporary measurements from XMM-Newton with its European Photon Imaging Camera (EPIC; suite of three CCDs: pn, MOS1, MOS2), and the Chandra X-ray Observatory with its Advanced CCD Imaging Spectrometer (ACIS).

ROSAT count rates (CR) were taken from mission catalogs (rass2rxs for the RASS; rospsc for PSPC pointings; roshri for HRI pointings) hosted by the High-Energy Astrophysics Science Archive Research Center (HEASARC) at the NASA Goddard Space Flight Center. The RASS exposure

times described below refer to the total of many brief scans during several days of sky coverage on the target, whereas the PSPC and HRI pointings were continuous integrations (modulo corrections for telemetry deadtime; likewise for the XMM and Chandra observations).

XMM and Chandra level-2 event lists (from HEASARC or the Chandra archive) were specially processed and measured according to protocols outlined by Ayres (2024). Counts inside an instrument-defined detection cell centered on the target were parsed into evenly-spaced time intervals, corrected for background, deadtime, and encircled energy factor. The time series was then subjected to a “flare filter” that removed percentages, possibly unequal, of the highest and lowest CR bins, according to a pre-defined elimination hierarchy. The “Olympic” filter suppressed transient enhancements (flares), as well as occasional dropouts (e.g., telemetry-saturating “background flares” for XMM). The adopted detection cells were 80% encircled energy for XMM (cell radius varied between $20''$ – $23''$ depending on EPIC module), and 95% for the higher resolution Chandra ACIS ($r = 1''.5$). These cell sizes were designed to maximize the source counts, while minimizing unwanted background events, based on the specific instrument characteristics.

Filtered average CR for XMM and Chandra, and catalog CR for ROSAT, were converted to X-ray fluxes at Earth using

an optimization scheme based on a grid of coronal emission-measure models (for details, see Ayres 2024). The output energy range was 0.1–2.4 keV (“ROSAT standard band”), for the unabsorbed flux (i.e., corrected for interstellar absorption). ISM column densities, N_{H} , for these nearby stars were set to a nominal $1 \times 10^{18} \text{ cm}^{-2}$. The adopted bandpass is well-suited to the spectral distributions of late-type coronal sources, and well-matched to the input energy ranges of the various X-ray missions considered here. Descriptions of the individual stellar measurements are given below.

2.2.1. X-Ray Luminosities

The K2 dwarf ϵ Eri (HD 22049) has been observed 17 times by XMM, mainly between 2015 February and 2022 January, but with a single earlier pointing in 2003 January. The exposures ranged from 7.6 ks to 21.5 ks, averaging 11 ks. Based on our new processing, the XMM time series had a mean $L_{\text{X}} = (19.1 \pm 3.5) \times 10^{27} \text{ erg s}^{-1}$, representing a time-average over multiple short activity cycles (2015–2022). Coffaro et al. (2020) and Fuhrmeister et al. (2023) have previously described most of the XMM pointings. Fuhrmeister et al. reported X-ray luminosities for seven additional XMM exposures obtained after the nine published by Coffaro et al., but apparently missing one from 2021 February. Combining the two time series yields $L_{\text{X}} = (19 \pm 4) \times 10^{27} \text{ erg s}^{-1}$, the same as our new processing of the full dataset. However, the agreement is probably coincidental because the earlier result refers to the narrower 0.2–2.0 keV energy band, and without flare filtering. Their result would be higher for our broader 0.1–2.4 keV energy band, but lower if the relatively few ϵ Eri flares were removed.

The K0 dwarf σ Dra (HD 185144) was observed several times in the ROSAT era: during the all-sky survey (1991 August, near cycle maximum) with a CR of 0.29 cps in 1.5 ks (deeper than normal owing to the high ecliptic latitude of the star, favored by the RASS scanning pattern); PSPC pointings near cycle maxima in 1992 November (0.17 cps in 2.7 ks) and 1997 February (0.37 cps in 1.7 ks); and a brief HRI exposure in 1998 April near cycle minimum (0.036 cps in 0.9 ks). X-ray luminosities derived from the various ROSAT measurements were in the range $(3.3\text{--}8.0) \times 10^{27} \text{ erg s}^{-1}$. We adopt the logarithmic average, $L_{\text{X}} = (5.1_{-1.4}^{+1.9}) \times 10^{27} \text{ erg s}^{-1}$. The variations exceed those seen in the extensive time series of the more active ϵ Eri, but are comparable to the larger swings of lower activity stars like α Cen B (HD 128621, K1V) and 61 Cyg A (HD 201091, K5V), which have more exaggerated starspot cycles in X-rays (see Ayres 2024). The influence of flares on the several ROSAT pointings is unknown, although such outbursts tend to be rare among the low-activity K dwarfs compared to their more active cousins.

The K1 dwarf 107 Psc (HD 10476) was not detected in the RASS, but there were two later ROSAT pointings: PSPC in

1993 July near cycle minimum (0.027 cps in 4.1 ks) and HRI in 1997 July near cycle maximum (0.0087 cps in 3.1 ks). The calibrated X-ray luminosities differ by a factor of two: $0.79 \times 10^{27} \text{ erg s}^{-1}$ for PSPC and $1.7 \times 10^{27} \text{ erg s}^{-1}$ for HRI. We adopt the logarithmic average $L_{\text{X}} = (1.2_{-0.4}^{+0.6}) \times 10^{27} \text{ erg s}^{-1}$, similar to 61 Cyg A (e.g., Ayres 2024).

The K1 dwarf HD 103095 was not detected in the RASS, but there were two subsequent ROSAT pointings: PSPC in 1993 May near cycle maximum (0.0055 cps in 2.8 ks), and HRI in 1996 November near cycle minimum (no detection in 6.7 ks). Chandra obtained one observation: 32.8 ks with ACIS-S in 2009 February near the mean activity level. The measured CR was only 0.0010 cps (consistent with the HRI non-detection). The calibrated X-ray luminosities of the ROSAT and Chandra detections differ by a factor of two: $0.21 \times 10^{27} \text{ erg s}^{-1}$ for PSPC and 0.13×10^{27} for ACIS-S. We adopt the logarithmic average, $L_{\text{X}} = (0.17_{-0.04}^{+0.05}) \times 10^{27} \text{ erg s}^{-1}$.

The K3 dwarf HD 219134 was detected in the RASS (1991 January, near cycle minimum) with a CR of 0.032 cps in 0.5 ks. The implied L_{X} is $(0.7 \pm 0.2) \times 10^{27} \text{ erg s}^{-1}$. There was also a 38 ks XMM pointing in 2016 June near the mean activity level. We adopt the XMM value (median of pn, MOS1, MOS2), $L_{\text{X}} = (0.72 \pm 0.05) \times 10^{27} \text{ erg s}^{-1}$, consistent with the RASS result but more precise due to the higher quality XMM instrumentation and the deeper exposure.

The K2 dwarf HD 166620 was not detected in the RASS, but there was a later HRI pointing in 1996 October near cycle maximum (0.0026 cps in 6.3 ks). The HRI CR implies $L_{\text{X}} = (1.1 \pm 0.3) \times 10^{27} \text{ erg s}^{-1}$, which we adopt for our analysis.

2.2.2. Mass-Loss Rates

Wind braking torques depend on the mass-loss rate and the Alfvén radius. Mass-loss rates are not directly measured in most of our targets, so we use the coronal heating rate (as inferred from X-ray luminosities) to estimate the mass-loss rates. Combining the X-ray luminosities adopted above and the SED radii determined below (Section 2.3), we calculated X-ray fluxes (F_{X}) for each of our targets. Wood et al. (2021) established an empirical relation between F_{X} and the mass-loss rate per unit surface area, $\dot{M} \propto F_{\text{X}}^{0.77 \pm 0.04}$. The mass-loss rates resulting from this empirical relation are shown in Table 1. For two of our targets (ϵ Eri and HD 219134 = GJ 892) we list the mass-loss rates directly inferred from Ly α measurements, as tabulated in Wood et al. (2021).

2.3. Stellar Properties

To obtain empirical constraints on the stellar luminosities, radii, and masses, we performed an analysis of the broadband SED of each star together with the Gaia DR3 parallaxes, following the procedures described in Stassun & Torres (2016) and Stassun et al. (2017, 2018). No systematic offset to the parallaxes was applied (see, e.g., Stassun & Torres 2021). Depending on the available published broadband

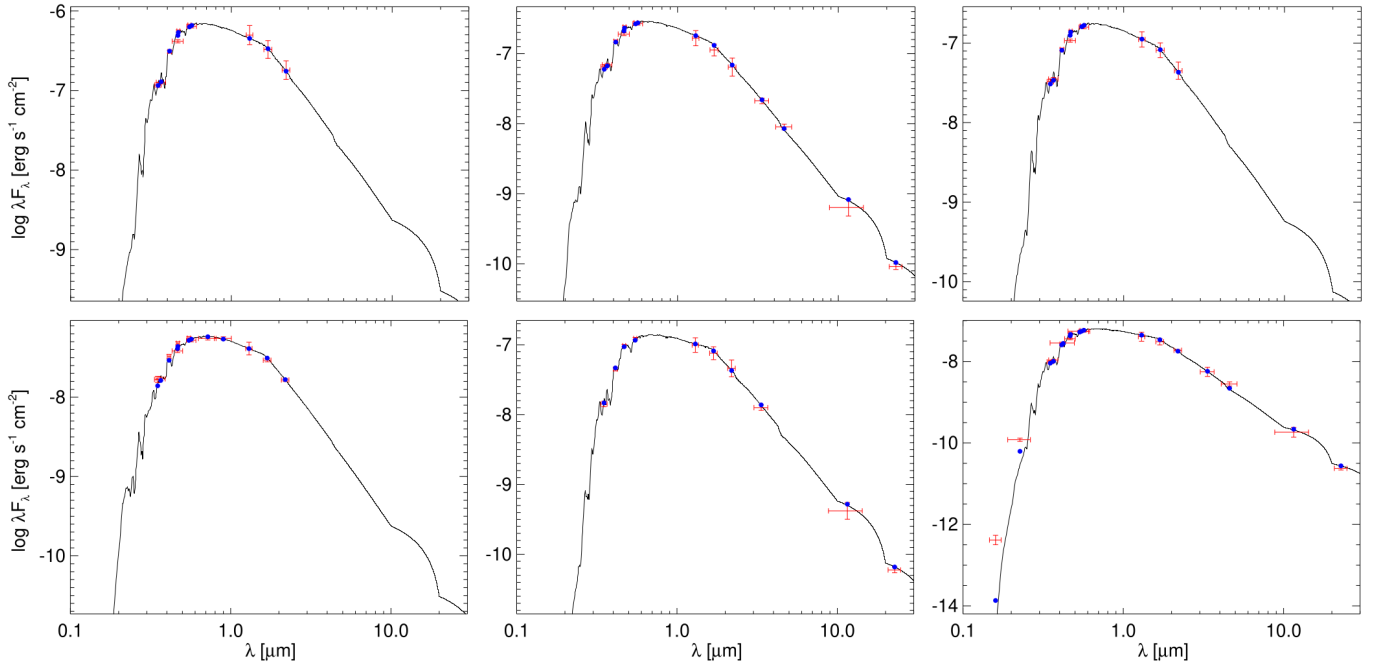


Figure 4. Spectral energy distributions of (top, left to right) ϵ Eri, σ Dra, and 107 Psc, and (bottom) HD 103095, HD 219134, and HD 166620. Red symbols represent the observed photometric measurements, and the horizontal bars represent the effective width of the bandpass. Blue symbols are the model fluxes from the best-fit Kurucz atmosphere model (black).

photometry for each star, we adopted some combination of the JHK_S magnitudes from 2MASS, the W1–W4 magnitudes from WISE, the UBV magnitudes from Mermilliod (2006), the Strömgen $ubvy$ magnitudes from Paunzen (2015), and the FUV and NUV magnitudes from GALEX. Together, the available photometry spans the full stellar SED over at least the wavelength range 0.4–10 μm in most cases, and in some cases as large as 0.2–20 μm (see Figure 4).

We performed a fit using Kurucz stellar atmosphere models, with the effective temperature T_{eff} , surface gravity $\log g$ and metallicity $[M/H]$ from the published spectroscopic analyses (see Table 1). The extinction A_V was fixed at zero in all cases due to the very close proximity of the stars. The resulting fits have a reduced $\chi^2 \approx 1$ in all cases. Integrating the model SED gives the bolometric flux at Earth, F_{bol} . Taking F_{bol} together with the Gaia parallax (Gaia Collaboration et al. 2021) yields the bolometric luminosity L_{bol} . The stellar radius then follows directly from the Stefan-Boltzmann relation. Finally, we estimate the stellar mass from the empirical eclipsing-binary based relations of Torres et al. (2010). The results are listed in Table 1.

3. INTERPRETATION

3.1. Rotational Evolution

We modeled the rotational evolution of our targets with an approach similar to that described in Metcalfe et al. (2023a,b, 2024b,c) with some minor amendments.

Our model grids are constructed with the Yale Rotating Evolution Code (YREC, see Pinsonneault et al. 1989) and

are identical to those described in Metcalfe et al. (2020) and van Saders & Pinsonneault (2013) with two notable modifications: first, we adopt the model atmospheres of Kurucz (1993) as boundary conditions, and second we include helium and heavy element diffusion and gravitational settling via the prescription of Thoul et al. (1994). In previous papers (Metcalfe et al. 2023a,b, 2024b,c; Saunders et al. 2024) we adopted an Eddington atmosphere over atmospheric tables to better match the asteroseismic modeling, which requires a detailed atmospheric structure. However, our target K dwarfs mostly lack asteroseismic detections and are sufficiently cool that a gray Eddington atmosphere is a particularly poor model. Because our target stars are both old and slowly rotating, we also opt to include diffusion and gravitational settling, as these processes can significantly impact the relationship between the observed surface metallicity and inferred bulk starting metallicity (Dotter et al. 2017). A solar calibration yields a solar bulk helium mass fraction of 0.2744, a mixing length of 1.967 pressure scale heights, and default Thoul et al. (1994) gravitational diffusion coefficients multiplied by 0.7326 to match the solar envelope helium abundance (Basu & Antia 1995). We adopt a chemical enrichment law of the form $Y = Y_p + \frac{dY}{dZ} Z$, with the primordial helium $Y_p = 0.249$ and $dY/dZ = (Y_\odot - Y_p)/Z_\odot = 1.352$. A solar model rotating at 25.4 days has a Rossby number in this model grid of $\text{Ro}_\odot = 2.36$.

In the absence of tight asteroseismic constraints for most targets, we used the rotational evolution model of Saunders et al. (2024) coupled with the constraints on radius, effective

temperature, surface metallicity, and rotation period to infer the stellar masses, ages, and Rossby numbers. This braking law includes the effects of WMB, but does not attempt to model the “stalled braking” observed in intermediate-age K dwarfs thought to be due to an epoch of internal angular momentum transport (Curtis et al. 2019, 2020; Spada & Lanzafame 2020). Neglecting this feature will tend to bias our model ages at $\sim 1\text{--}2$ Gyr, in the sense that our ages should appear younger than those inferred from models that include the stalled braking. The effect on old stars is modest, and in all cases our approach should preserve the rank-ordering of systems in age and Rossby number.

We adopted the observational constraints and their associated uncertainties from Table 1. We inflated the reported random errors with systematic error estimates added in quadrature: 2% in T_{eff} and 4.2% in radius following the recommendation of Tayar et al. (2022), 0.1 dex in surface abundance, and 10% in period (Epstein & Pinsonneault 2014). We placed broad Gaussian priors (specified as a central value and a 1σ width) on the stellar masses ($0.8 \pm 0.2 M_{\odot}$), bulk abundance (± 0.5 dex centered on the observed surface abundance), age (4.5 ± 5 Gyr) and mixing length α (1.5 ± 0.5) for all target stars. We adopted the braking law parameters from Saunders et al. (2024), appropriately re-normalized to reflect the slightly different solar convective overturn timescale and photospheric pressure in the new model grid.

We validated our modeling procedure against other age inference techniques. We inferred rotation-based ages for three asteroseismic targets of similar surface temperatures with precise ages from Saunders et al. (2024)—KIC 11772920, KIC 9025370, and KIC 7970740. Our non-seismic, rotation-based ages using the WMB model agree with the quoted asteroseismic ages within 0.8σ , 1.2σ , and 0.8σ , respectively, with the caveat that these stars were themselves utilized in the Saunders et al. (2024) calibration process. For the two K dwarfs in our sample with asteroseismic ages (which were not used as priors in the fit), our WMB rotation-based ages agree with the asteroseismic values within 1σ . Cool K dwarfs evolve slowly, and therefore cannot be age-dated with standard isochrone methods. Isochrone fitting for our target stars with the YREC model grid yielded uninformative ages, as expected given their positions near the main-sequence.

A gyrochronology model $\text{GP}_{\text{gyro}}^1$ (Lu et al. 2024) calibrated on gyro-kinematic ages (Lu et al. 2021) with rotation measurements from Kepler (McQuillan et al. 2014; Santos et al. 2019), and ZTF (Lu et al. 2022) was also used to infer ages for the targets. Gyro-kinematic ages use samples of stars selected to have similar rotation periods, temperature, and absolute Gaia G magnitude to define mono-age kinematic

sets, instead of the traditional selection in physical space. As such, the method performs well in populations where the spin-down is simple, but may provide biased ages when stars of different ages can have similar rotation periods—such as objects undergoing WMB or stalled braking. Our WMB ages agree within 1σ for 107 Psc, HD 219134, and HD 166620. They agree within 2.2σ for ϵ Eri, 1.7σ for σ Dra, and 1.8σ for HD 103095. Gyro-kinematic ages are known to have issues for stars as young as ϵ Eri, and do not explicitly account for metallicity, which may help to explain σ Dra and HD 103095. Agreement in the old, solar metallicity targets is excellent.

Model ages are provided in Table 1 for both the assumption of standard spin-down (“Age, gyro”) and weakened magnetic braking (“Age, WMB”). Rossby numbers for the two cases are identical within their uncertainties, and are computed using the observed rotation period and the model convective overturn timescale for the WMB case. Formally, some of these stars are just slightly below the threshold of $\text{Ro}_{\text{crit}} = 0.91 \pm 0.03(\text{rand}) \pm 0.03(\text{sys}) \text{Ro}_{\odot}$ identified in Saunders et al. (2024), although we caution against a strict interpretation. Saunders et al. (2024) found that their fit for the value of Ro_{crit} depended on assumptions about helium abundances in the model grid, and they had very few calibrator stars in this mass and effective temperature range. Furthermore, the standard braking timescales for stars near the onset of WMB are long. For example, the period of 107 Psc will only change by 20% in 2.5 Gyr—so the surface rotation periods (and thus period-based ages) of K dwarfs will not deviate from the standard spin-down case until later in their evolution, even if their surface torques have dropped significantly.

3.2. Wind Braking Torque

In Section 2 we obtained constraints on most of the inputs that are required to calculate the wind braking torque using the prescription of Finley & Matt (2018)². Spectropolarimetry provided constraints on the equivalent polar field strengths for the large-scale magnetic field (B_d, B_q, B_o), archival X-ray measurements produced estimates of mass-loss rates from the empirical relation of Wood et al. (2021), and SED fitting yielded stellar radii and masses. In this section we combine these inputs with rotation periods measured from the Mount Wilson survey (Baliunas et al. 1996), and from Folsom et al. (2018a) for HD 219134, to estimate the wind braking torque for each of our targets. We also evaluate the relative importance of various contributions to the overall decrease in the torque along the evolutionary sequence. The resulting estimates of wind braking torque are listed in Table 1 and illustrated in Figure 5, with uncertainties defined by simultaneously shifting all of the inputs within their 1σ uncertainties to minimize or maximize the torque.

¹ Available at <https://github.com/lyx12311/GPgyro>

² <https://github.com/travismetcalf/FinleyMatt2018>

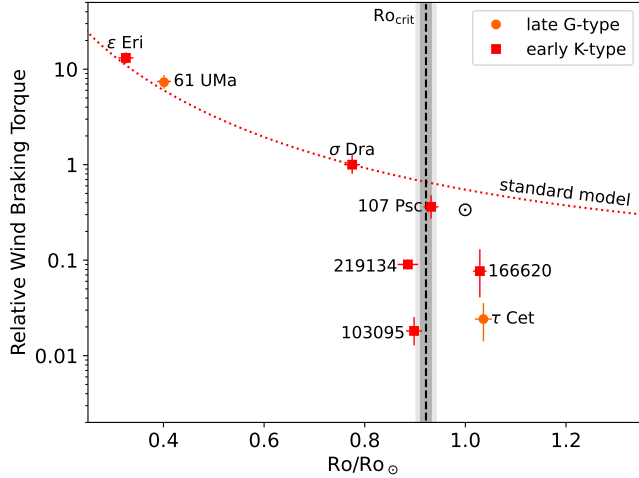


Figure 5. Estimated wind braking torque relative to σ Dra as a function of Ro normalized to the solar value. Points are coded by spectral type as shown in the legend. The light gray shaded area indicates the systematic uncertainty in Ro/Ro_{\odot} , while the darker gray shaded area marks the empirical onset of WMB in solar analogs.

For previous samples of hotter stars, we adopted the asteroseismic calibration of convective overturn times from Corsaro et al. (2021) to calculate Rossby numbers. Unfortunately, this relation is only calibrated for Gaia colors between $0.55 < G_{BP} - G_{RP} < 0.97$, and all of the stars in our K dwarf sample are redder. Metcalfe et al. (2024a) recently extended the relation to redder colors, using measured rotation periods and mean activity levels from the Mount Wilson survey to estimate the convective overturn times. The results suggested that the observed deviation from linearity in Corsaro et al. (2021) at $G_{BP} - G_{RP} > 0.85$ was probably an observational bias against the detection of solar-like oscillations in more active K-type stars. The extended relation is nearly linear between $0.55 < G_{BP} - G_{RP} < 1.2$, and allows us to estimate Ro/Ro_{\odot} from the inverse of the mean activity level relative to the solar value from Egeland et al. (2017). We use this formulation to estimate Ro/Ro_{\odot} for the early K-type stars in our sample, as well as the late G-type stars from Metcalfe et al. (2023a), yielding values that are consistent with rotation-based estimates (see Table 1).

To establish a context for our estimated wind braking torques, Figure 5 includes a standard spin-down model for σ Dra (red dotted line), as well as the empirical value of Ro_{crit} for the onset of WMB in solar analogs (Metcalfe et al. 2022). The targets with Ro/Ro_{\odot} well below Ro_{crit} are consistent with the standard spin-down model, while those near and above Ro_{crit} show varying degrees of WMB (discussed below). The most evolved stars in Figure 5—the magnetic grand minimum star HD 166620, and the flat activity star τ Cet—are well beyond Ro_{crit} and have estimated wind braking torques that are substantially below the standard spin-down predictions. This pattern broadly corroborates our find-

ings from similar wind braking estimates for hotter stars (Metcalfe et al. 2021, 2022, 2023a, 2024b).

Our wind braking estimate for ϵ Eri adopts a direct inference of the mass-loss rate from $Ly\alpha$ measurements. The mass-loss rate implied by the X-ray luminosity and stellar radius listed in Table 1 is somewhat lower than the direct inference ($9.9_{-2.5}^{+3.3} \dot{M}_{\odot}$), which would yield a weaker torque ($7.6_{-1.8}^{+2.4} \times 10^{30}$ erg) comparable to 61 UMa in Figure 5. Considering the lower metallicity of σ Dra, the resulting deviation from the standard spin-down model would not fundamentally alter our interpretation (e.g., see Amard et al. 2020).

The most evolved target that has not yet entered the WMB regime is σ Dra, with a wind braking torque that is more than an order of magnitude weaker than ϵ Eri (-92%). To assess the relative importance of various contributions to the overall decrease in the wind braking torque, we can modify one parameter at a time between the fiducial models for these two stars. We assume that magnetic field strength scales with the observed $\log \langle R'_{HK} \rangle$ and is reflected in the absolute values of (B_d, B_q, B_o) , while the field morphology is reflected in their relative values. As expected for standard spin-down, the total decrease in wind braking torque is dominated by evolutionary changes in the mass-loss rate (-71%), magnetic field strength and morphology (-58%), and rotation period (-56%). These contributions are slightly offset by differences in the stellar radius ($+40\%$) and mass ($+0.5\%$). For this pair of stars, the combined influence of field strength and morphology is dominated by evolutionary changes in magnetic field strength (-55%) with a very small contribution from differences in morphology (-7%).

The youngest target that may have recently entered the WMB regime is 107 Psc, with a wind braking torque several times weaker than σ Dra (-64%) falling slightly below the standard spin-down prediction. Comparing the fiducial models for these two stars, the total decrease in wind braking torque is once again dominated by evolutionary changes in the mass-loss rate (-47%), magnetic field strength and morphology (-23%), and rotation period (-23%), with a small contribution from the difference in stellar mass (-0.8%) offset by the difference in radius ($+18\%$). In this case, the combined influence of field strength and morphology is still primarily from evolutionary changes in magnetic field strength (-16%), but with a comparable contribution due to changes in morphology (-9%).

Our most evolved target with a ZDI map is HD 219134, which has a wind braking torque more than an order of magnitude weaker than σ Dra (-91%), well within the WMB regime. For this pair of stars, the total decrease in wind braking torque is still dominated by evolutionary changes in the mass-loss rate (-62%), magnetic field strength and morphology (-55%), and rotation period (-36%). These contributions are reinforced in this case by differences in the stellar

radius (−18%), and slightly offset by a small difference in mass (+1.1%). In contrast to our evolutionary sequence in the standard spin-down regime, the combined influence of field strength and morphology is now dominated by differences in morphology (−49%) with a much smaller contribution from differences in magnetic field strength (−12%). Like ϵ Eri, the fiducial model for HD 219134 adopts a direct inference of the mass-loss rate from Ly α measurements. The mass-loss rate implied by the X-ray luminosity and stellar radius listed in Table 1 is higher ($0.75^{+0.07}_{-0.08} \dot{M}_{\odot}$), which would yield a slightly stronger torque ($0.119^{+0.019}_{-0.018} \times 10^{30}$ erg) that would shift the point upwards in Figure 5 by roughly its own size. This would reduce the relative importance of changes in the mass-loss rate (from −62% to −53%) without altering our other conclusions.

For the final two targets in our sample (HD 103095 and HD 166620) we have made the conservative assumption that all of the large-scale field is in an axisymmetric dipole configuration. This prevents us from drawing firm conclusions about changes in the magnetic morphology relative to field strength, but we can still assess the importance of other changes. The estimated wind braking torque for HD 103095 is more than fifty times weaker than σ Dra (−98%), a decrease that might be enhanced by the extreme low metallicity of this star (as suggested previously by metal-poor τ Cet). In this case, the total decrease in wind braking torque is dominated by evolutionary changes in the magnetic field strength and morphology (−88%), mass-loss rate (−72%), and rotation period (−13%), reinforced by differences in stellar radius (−44%) and offset by differences in the mass (+8%).

The oldest star in our sample is HD 166620, with a wind braking torque that is more than an order of magnitude weaker than σ Dra (−92%). As with HD 103095, the total decrease in wind braking torque is dominated by evolutionary changes in the magnetic field strength and morphology (−78%), mass-loss rate (−48%), and rotation period (−37%). These contributions are slightly offset by differences in the stellar radius (+4%) and mass (+1.1%). For both HD 103095 and HD 166620, note that the combined influence of field strength and morphology may be even more important if the magnetic field is actually comprised of a mixture of dipole, quadrupole, and octupole components.

4. SUMMARY AND DISCUSSION

We have assembled new and archival observations (Section 2) to estimate the wind braking torque for an evolutionary sequence of six early K-type stars using the prescription of Finley & Matt (2018). The resulting constraints on magnetic braking (Table 1) complement our earlier applications to two late F-type stars (Metcalfe et al. 2021), five solar analogs (Metcalfe et al. 2022, 2024b), and two late G-type stars (Metcalfe et al. 2023a), gradually extending the

approach to the more challenging cooler targets. The evolutionary picture that emerges (Section 3) is broadly consistent with our previous findings, revealing a dramatic transition from the relatively well calibrated standard spin-down behavior in more active stars like ϵ Eri and σ Dra to substantially weakened braking in the least active targets like the magnetic grand minimum star HD 166620 (Figure 5).

As with the hotter targets, the wind braking torque in early K-type stars decreases by roughly an order of magnitude as they reach a critical value of the Rossby number ($\text{Ro}_{\text{crit}} \sim 0.9 \text{ Ro}_{\odot}$). We observe a drop in both magnetic field strength and X-ray luminosity across this boundary. The onset of WMB occurs at the same Ro_{crit} as the threshold for hotter stars, even though the characteristic rotation periods for post-transition stars are significantly longer here (31–43 days), compared to 21–23 days for solar analogs (Metcalfe et al. 2022, 2024b) and even shorter for late F-type stars (Metcalfe et al. 2019, 2021). Our finding confirms the Rossby number as the key global stellar predictor of WMB.

The larger number of targets, and the longer evolutionary timescales of K dwarfs, have allowed us to probe the onset of WMB in greater detail than we could in the hotter stars. For the first time, we may have caught one star (107 Psc) on the cusp of the transition from standard spin-down to WMB, showing a moderately reduced braking torque driven primarily by weaker mass-loss with a smaller contribution from magnetic properties and rotation. In the standard spin-down regime (from ϵ Eri to σ Dra) the contribution of magnetic properties to the evolution of wind braking torque can be attributed almost entirely to changes in the field strength (−55%), with very little change in magnetic morphology (−7%). By contrast, in the WMB regime (from σ Dra to HD 219134) the magnetic contributions are almost reversed, with a large decrease in wind braking torque due to a magnetic morphology shift (−49%) and very little change due to field strength (−12%). Understanding how this apparent trend continues to evolve within the WMB regime will require detailed ZDI mapping of older targets such as HD 166620, which is in a prolonged flat activity phase and shows extremely small variations in circular polarization.

The ubiquity of stellar activity cycles in this sample is a natural consequence of the longer evolutionary timescales of K dwarfs and the finite age of the Galaxy. In a similar sample of solar analogs, we found one star in the WMB regime with an activity cycle (18 Sco; Metcalfe et al. 2022), while older stars in that sample (16 Cyg A and 16 Cyg B) showed constant activity over decades (Radick et al. 2018). This is consistent with previous suggestions that the onset of WMB corresponds to the disruption of large-scale organization by the stellar dynamo, with activity cycles growing longer and weaker over roughly the second half of main-sequence lifetimes (Metcalfe & van Saders 2017). In contrast to our hotter

targets, there are no observations of “flat activity” among the K stars (Baliunas et al. 1995). The only apparent exception is the K-type subgiant δ Eri, which originated as an F-type star on the main-sequence (Carrier et al. 2003).

The fact that the WMB regime only begins after ~ 7 Gyr in K dwarfs, combined with their longer main-sequence lifetimes, implies that even the oldest stars in our sample are still in the early phases of this magnetic transition. As a consequence, activity cycles are still evident in the K dwarfs that exhibit WMB—with the exception of HD 166620, which transitioned from cycling to flat activity near the end of the Mount Wilson survey (Baum et al. 2022; Luhn et al. 2022). If the value of Ro_{crit} for the onset of WMB is also the critical value for the efficient operation of a large-scale dynamo (Durney & Latour 1978; Metcalfe et al. 2020, 2024c), then the activity cycles in K dwarfs older than ~ 7 Gyr may represent subcritical stellar dynamos (Tripathi et al. 2021).

Future observations promise to improve our characterization of the transition to WMB in this sample of early K-type stars. Direct inferences of the mass-loss rate for σ Dra and HD 166620 may be possible from $Ly\alpha$ measurements, and the required Hubble Space Telescope observations have already been approved (HST-GO-17793, PI: B. Wood). Even in the absence of a mass-loss detection for HD 166620, an updated X-ray luminosity may soon emerge from an approved 34 ks XMM observation (PI: B. Stelzer), which can be compared to our ROSAT-era measurement while it was still cycling in the 1990s. Time series spectropolarimetry of HD 166620 and τ Cet for the construction of ZDI maps will be challenging—both because of the tiny Stokes V variations (e.g., Figure 1), and the longer rotation periods that require

sustained observing campaigns—but the effort is justified by the relatively unexplored domain at high Rossby number that they seem to occupy.

The authors would like to thank Tim Brown, Ricky Ege-land, and Brian Wood for helpful exchanges. T.S.M. acknowledges support from NSF grant AST-2205919 and NASA grant 80NSSC22K0475. Computational time at the Texas Advanced Computing Center was provided through allocation TG-AST090107. J.v.S. acknowledges support from NSF grant AST-2205888. O.K. acknowledges support by the Swedish Research Council (grant agreements no. 2019-03548 and 2023-03667). K.G.S. acknowledges funding for PEPSI (<https://pepsi.aip.de/>) through the German Verbundforschung grants 05AL2BA1/3 and 05A08BAC as well as the State of Brandenburg. A.J.F. acknowledges support from the European Research Council (ERC) under the European Union’s Horizon 2020 research and innovation program (grant agreement No. 810218 WHOLESUN). R.A.G. acknowledges support from the PLATO and GOLF Centre National D’Études Spatiales grants. The LBT is an international collaboration among institutions in the United States, Italy and Germany. LBT Corporation partners are: The University of Arizona on behalf of the Arizona Board of Regents; Istituto Nazionale di Astrofisica, Italy; LBT Beteiligungsgesellschaft, Germany, representing the Max-Planck Society, The Leibniz Institute for Astrophysics Potsdam, and Heidelberg University; The Ohio State University, and The Research Corporation, on behalf of The University of Notre Dame, University of Minnesota and University of Virginia.

REFERENCES

- Amard, L., Roquette, J., & Matt, S. P. 2020, *MNRAS*, 499, 3481, doi: [10.1093/mnras/staa3038](https://doi.org/10.1093/mnras/staa3038)
- Aurière, M. 2003, in *EAS Publications Series*, Vol. 9, *EAS Publications Series*, ed. J. Arnaud & N. Meunier, 105
- Ayres, T. 2024, *AJ*, submitted
- Baliunas, S., Sokoloff, D., & Soon, W. 1996, *ApJL*, 457, L99, doi: [10.1086/309891](https://doi.org/10.1086/309891)
- Baliunas, S. L., Donahue, R. A., Soon, W. H., et al. 1995, *ApJ*, 438, 269, doi: [10.1086/175072](https://doi.org/10.1086/175072)
- Basu, S., & Antia, H. M. 1995, *MNRAS*, 276, 1402, doi: [10.1093/mnras/276.4.1402](https://doi.org/10.1093/mnras/276.4.1402)
- Baum, A. C., Wright, J. T., Luhn, J. K., & Isaacson, H. 2022, *AJ*, 163, 183, doi: [10.3847/1538-3881/ac5683](https://doi.org/10.3847/1538-3881/ac5683)
- Bellotti, S., Morin, J., Lehmann, L. T., et al. 2024, *A&A*, 686, A66, doi: [10.1051/0004-6361/202348043](https://doi.org/10.1051/0004-6361/202348043)
- Boro Saikia, S., Lueftinger, T., Jeffers, S. V., et al. 2018, *A&A*, 620, L11, doi: [10.1051/0004-6361/201834347](https://doi.org/10.1051/0004-6361/201834347)
- Bowler, B. P., Tran, Q. H., Zhang, Z., et al. 2023, *AJ*, 165, 164, doi: [10.3847/1538-3881/acbd34](https://doi.org/10.3847/1538-3881/acbd34)
- Brewer, J. M., Fischer, D. A., Valenti, J. A., & Piskunov, N. 2016, *ApJS*, 225, 32, doi: [10.3847/0067-0049/225/2/32](https://doi.org/10.3847/0067-0049/225/2/32)
- Brown, T. M. 2014, *ApJ*, 789, 101, doi: [10.1088/0004-637X/789/2/101](https://doi.org/10.1088/0004-637X/789/2/101)
- Brun, A. S., Strugarek, A., Noraz, Q., et al. 2022, *ApJ*, 926, 21, doi: [10.3847/1538-4357/ac469b](https://doi.org/10.3847/1538-4357/ac469b)
- Buzasi, D. L. 1997, *ApJ*, 484, 855, doi: [10.1086/304374](https://doi.org/10.1086/304374)
- Cao, L., & Pinsonneault, M. H. 2022, *MNRAS*, 517, 2165, doi: [10.1093/mnras/stac2706](https://doi.org/10.1093/mnras/stac2706)
- Carrier, F., Bouchy, F., & Eggenberger, P. 2003, in *Asteroseismology Across the HR Diagram*, ed. M. J. Thompson, M. S. Cunha, & M. J. P. F. G. Monteiro, Vol. 284, 311–314
- Coffaro, M., Stelzer, B., Orlando, S., et al. 2020, *A&A*, 636, A49, doi: [10.1051/0004-6361/201936479](https://doi.org/10.1051/0004-6361/201936479)

- Corsaro, E., Bonanno, A., Mathur, S., et al. 2021, *A&A*, 652, L2, doi: [10.1051/0004-6361/202141395](https://doi.org/10.1051/0004-6361/202141395)
- Curtis, J. L., Agüeros, M. A., Douglas, S. T., & Meibom, S. 2019, *ApJ*, 879, 49, doi: [10.3847/1538-4357/ab2393](https://doi.org/10.3847/1538-4357/ab2393)
- Curtis, J. L., Agüeros, M. A., Matt, S. P., et al. 2020, *ApJ*, 904, 140, doi: [10.3847/1538-4357/abfb58](https://doi.org/10.3847/1538-4357/abfb58)
- David, T. J., Angus, R., Curtis, J. L., et al. 2022, *ApJ*, 933, 114, doi: [10.3847/1538-4357/ac6dd3](https://doi.org/10.3847/1538-4357/ac6dd3)
- do Nascimento, J. D., Barnes, S. A., Saar, S. H., et al. 2023, *ApJ*, 958, 57, doi: [10.3847/1538-4357/acfc1a](https://doi.org/10.3847/1538-4357/acfc1a)
- Donati, J. F., Semel, M., Carter, B. D., Rees, D. E., & Collier Cameron, A. 1997, *MNRAS*, 291, 658, doi: [10.1093/mnras/291.4.658](https://doi.org/10.1093/mnras/291.4.658)
- Donati, J. F., Howarth, I. D., Jardine, M. M., et al. 2006, *MNRAS*, 370, 629, doi: [10.1111/j.1365-2966.2006.10558.x](https://doi.org/10.1111/j.1365-2966.2006.10558.x)
- Dotter, A., Conroy, C., Cargile, P., & Asplund, M. 2017, *ApJ*, 840, 99, doi: [10.3847/1538-4357/aa6d10](https://doi.org/10.3847/1538-4357/aa6d10)
- Durney, B. R., & Latour, J. 1978, *Geophysical and Astrophysical Fluid Dynamics*, 9, 241, doi: [10.1080/03091927708242330](https://doi.org/10.1080/03091927708242330)
- Egeland, R., Soon, W., Baliunas, S., et al. 2017, *ApJ*, 835, 25, doi: [10.3847/1538-4357/835/1/25](https://doi.org/10.3847/1538-4357/835/1/25)
- Epstein, C. R., & Pinsonneault, M. H. 2014, *ApJ*, 780, 159, doi: [10.1088/0004-637X/780/2/159](https://doi.org/10.1088/0004-637X/780/2/159)
- Finley, A. J., & Matt, S. P. 2018, *ApJ*, 854, 78, doi: [10.3847/1538-4357/aaaab5](https://doi.org/10.3847/1538-4357/aaaab5)
- Folsom, C. P., Fossati, L., Wood, B. E., et al. 2018a, *MNRAS*, 481, 5286, doi: [10.1093/mnras/sty2494](https://doi.org/10.1093/mnras/sty2494)
- Folsom, C. P., Bouvier, J., Petit, P., et al. 2018b, *MNRAS*, 474, 4956, doi: [10.1093/mnras/stx3021](https://doi.org/10.1093/mnras/stx3021)
- Fuhrmeister, B., Coffaro, M., Stelzer, B., et al. 2023, *A&A*, 672, A149, doi: [10.1051/0004-6361/202245201](https://doi.org/10.1051/0004-6361/202245201)
- Gaia Collaboration, Brown, A. G. A., Vallenari, A., et al. 2021, *A&A*, 649, A1, doi: [10.1051/0004-6361/202039657](https://doi.org/10.1051/0004-6361/202039657)
- García, R. A., Ceillier, T., Salabert, D., et al. 2014, *A&A*, 572, A34, doi: [10.1051/0004-6361/201423888](https://doi.org/10.1051/0004-6361/201423888)
- Garraffo, C., Drake, J. J., & Cohen, O. 2016, *A&A*, 595, A110, doi: [10.1051/0004-6361/201628367](https://doi.org/10.1051/0004-6361/201628367)
- Garraffo, C., Drake, J. J., Dotter, A., et al. 2018, *ApJ*, 862, 90, doi: [10.3847/1538-4357/aace5d](https://doi.org/10.3847/1538-4357/aace5d)
- Hall, O. J., Davies, G. R., van Saders, J., et al. 2021, *Nature Astronomy*, 5, 707, doi: [10.1038/s41550-021-01335-x](https://doi.org/10.1038/s41550-021-01335-x)
- Hon, M., Huber, D., Li, Y., et al. 2024, *ApJ*, 975, 147, doi: [10.3847/1538-4357/ad76a9](https://doi.org/10.3847/1538-4357/ad76a9)
- Jeffers, S. V., Petit, P., Marsden, S. C., et al. 2014, *A&A*, 569, A79, doi: [10.1051/0004-6361/201423725](https://doi.org/10.1051/0004-6361/201423725)
- Johnson, M. C., Endl, M., Cochran, W. D., et al. 2016, *ApJ*, 821, 74, doi: [10.3847/0004-637X/821/2/74](https://doi.org/10.3847/0004-637X/821/2/74)
- Kawaler, S. D. 1988, *ApJ*, 333, 236, doi: [10.1086/166740](https://doi.org/10.1086/166740)
- Kochukhov, O., Makaganiuk, V., & Piskunov, N. 2010, *A&A*, 524, A5, doi: [10.1051/0004-6361/201015429](https://doi.org/10.1051/0004-6361/201015429)
- Kurucz, R. L. 1993, in *Astronomical Society of the Pacific Conference Series*, Vol. 44, IAU Colloq. 138: Peculiar versus Normal Phenomena in A-type and Related Stars, ed. M. M. Dworetsky, F. Castelli, & R. Faraggiana, 87
- Li, Y., Huber, D., van Saders, J., et al. 2025, *ApJ*, submitted
- Lu, Y., Angus, R., Foreman-Mackey, D., & Hattori, S. 2024, *AJ*, 167, 159, doi: [10.3847/1538-3881/ad28b9](https://doi.org/10.3847/1538-3881/ad28b9)
- Lu, Y. L., Angus, R., Curtis, J. L., David, T. J., & Kiman, R. 2021, *AJ*, 161, 189, doi: [10.3847/1538-3881/abe4d6](https://doi.org/10.3847/1538-3881/abe4d6)
- Lu, Y. L., Curtis, J. L., Angus, R., David, T. J., & Hattori, S. 2022, *AJ*, 164, 251, doi: [10.3847/1538-3881/ac9bee](https://doi.org/10.3847/1538-3881/ac9bee)
- Luhn, J. K., Wright, J. T., Henry, G. W., Saar, S. H., & Baum, A. C. 2022, *ApJL*, 936, L23, doi: [10.3847/2041-8213/ac8b13](https://doi.org/10.3847/2041-8213/ac8b13)
- Masuda, K. 2022, *ApJ*, 937, 94, doi: [10.3847/1538-4357/ac8d58](https://doi.org/10.3847/1538-4357/ac8d58)
- McQuillan, A., Mazeh, T., & Aigrain, S. 2014, *ApJS*, 211, 24, doi: [10.1088/0067-0049/211/2/24](https://doi.org/10.1088/0067-0049/211/2/24)
- Mermilliod, J. C. 2006, *VizieR Online Data Catalog*, II/168
- Metcalf, T. S., Corsaro, E., Bonanno, A., Creevey, O. L., & van Saders, J. L. 2024a, *RNAAS*, 8, 260, doi: [10.3847/2515-5172/ad8566](https://doi.org/10.3847/2515-5172/ad8566)
- Metcalf, T. S., Kochukhov, O., Ilyin, I. V., et al. 2019, *ApJL*, 887, L38, doi: [10.3847/2041-8213/ab5e48](https://doi.org/10.3847/2041-8213/ab5e48)
- Metcalf, T. S., & van Saders, J. 2017, *SoPh*, 292, 126, doi: [10.1007/s11207-017-1157-5](https://doi.org/10.1007/s11207-017-1157-5)
- Metcalf, T. S., Buccino, A. P., Brown, B. P., et al. 2013, *ApJL*, 763, L26, doi: [10.1088/2041-8205/763/2/L26](https://doi.org/10.1088/2041-8205/763/2/L26)
- Metcalf, T. S., Creevey, O. L., Doğan, G., et al. 2014, *ApJS*, 214, 27, doi: [10.1088/0067-0049/214/2/27](https://doi.org/10.1088/0067-0049/214/2/27)
- Metcalf, T. S., van Saders, J. L., Basu, S., et al. 2020, *ApJ*, 900, 154, doi: [10.3847/1538-4357/aba963](https://doi.org/10.3847/1538-4357/aba963)
- . 2021, *ApJ*, 921, 122, doi: [10.3847/1538-4357/ac1f19](https://doi.org/10.3847/1538-4357/ac1f19)
- Metcalf, T. S., Finley, A. J., Kochukhov, O., et al. 2022, *ApJL*, 933, L17, doi: [10.3847/2041-8213/ac794d](https://doi.org/10.3847/2041-8213/ac794d)
- Metcalf, T. S., Strassmeier, K. G., Ilyin, I. V., et al. 2023a, *ApJL*, 948, L6, doi: [10.3847/2041-8213/acce38](https://doi.org/10.3847/2041-8213/acce38)
- Metcalf, T. S., Buzasi, D., Huber, D., et al. 2023b, *AJ*, 166, 167, doi: [10.3847/1538-3881/acf1f7](https://doi.org/10.3847/1538-3881/acf1f7)
- Metcalf, T. S., Strassmeier, K. G., Ilyin, I. V., et al. 2024b, *ApJL*, 960, L6, doi: [10.3847/2041-8213/ad0a95](https://doi.org/10.3847/2041-8213/ad0a95)
- Metcalf, T. S., van Saders, J. L., Huber, D., et al. 2024c, *ApJ*, 974, 31, doi: [10.3847/1538-4357/ad6dd6](https://doi.org/10.3847/1538-4357/ad6dd6)
- Noyes, R. W., Hartmann, L. W., Baliunas, S. L., Duncan, D. K., & Vaughan, A. H. 1984, *ApJ*, 279, 763, doi: [10.1086/161945](https://doi.org/10.1086/161945)
- Paunzen, E. 2015, *A&A*, 580, A23, doi: [10.1051/0004-6361/201526413](https://doi.org/10.1051/0004-6361/201526413)
- Petit, P., Louge, T., Théado, S., et al. 2014, *PASP*, 126, 469, doi: [10.1086/676976](https://doi.org/10.1086/676976)
- Petit, P., Folsom, C. P., Donati, J. F., et al. 2021, *A&A*, 648, A55, doi: [10.1051/0004-6361/202040027](https://doi.org/10.1051/0004-6361/202040027)

- Pinsonneault, M. H., Kawaler, S. D., Sofia, S., & Demarque, P. 1989, *ApJ*, 338, 424, doi: [10.1086/167210](https://doi.org/10.1086/167210)
- Radick, R. R., Lockwood, G. W., Henry, G. W., Hall, J. C., & Pevtsov, A. A. 2018, *ApJ*, 855, 75, doi: [10.3847/1538-4357/aaaee3](https://doi.org/10.3847/1538-4357/aaaee3)
- Reiners, A., Shulyak, D., Käpylä, P. J., et al. 2022, *A&A*, 662, A41, doi: [10.1051/0004-6361/202243251](https://doi.org/10.1051/0004-6361/202243251)
- Ryabchikova, T., Piskunov, N., Kurucz, R. L., et al. 2015, *PhysS*, 90, 054005, doi: [10.1088/0031-8949/90/5/054005](https://doi.org/10.1088/0031-8949/90/5/054005)
- Santos, A. R. G., García, R. A., Mathur, S., et al. 2019, *ApJS*, 244, 21, doi: [10.3847/1538-4365/ab3b56](https://doi.org/10.3847/1538-4365/ab3b56)
- Saunders, N., van Saders, J. L., Lyttle, A. J., et al. 2024, *ApJ*, 962, 138, doi: [10.3847/1538-4357/ad1516](https://doi.org/10.3847/1538-4357/ad1516)
- See, V., Jardine, M., Vidotto, A. A., et al. 2016, *MNRAS*, 462, 4442, doi: [10.1093/mnras/stw2010](https://doi.org/10.1093/mnras/stw2010)
- Semel, M. 1989, *A&A*, 225, 456
- Skumanich, A. 1972, *ApJ*, 171, 565, doi: [10.1086/151310](https://doi.org/10.1086/151310)
- Spada, F., & Lanzafame, A. C. 2020, *A&A*, 636, A76, doi: [10.1051/0004-6361/201936384](https://doi.org/10.1051/0004-6361/201936384)
- Stassun, K. G., Collins, K. A., & Gaudi, B. S. 2017, *AJ*, 153, 136, doi: [10.3847/1538-3881/aa5df3](https://doi.org/10.3847/1538-3881/aa5df3)
- Stassun, K. G., Corsaro, E., Pepper, J. A., & Gaudi, B. S. 2018, *AJ*, 155, 22, doi: [10.3847/1538-3881/aa998a](https://doi.org/10.3847/1538-3881/aa998a)
- Stassun, K. G., & Torres, G. 2016, *ApJL*, 831, L6, doi: [10.3847/2041-8205/831/1/L6](https://doi.org/10.3847/2041-8205/831/1/L6)
- . 2021, *ApJL*, 907, L33, doi: [10.3847/2041-8213/abdaad](https://doi.org/10.3847/2041-8213/abdaad)
- Strassmeier, K. G., Ilyin, I., Järvinen, A., et al. 2015, *Astronomische Nachrichten*, 336, 324, doi: [10.1002/asna.201512172](https://doi.org/10.1002/asna.201512172)
- Tayar, J., Claytor, Z. R., Huber, D., & van Saders, J. 2022, *ApJ*, 927, 31, doi: [10.3847/1538-4357/ac4bbc](https://doi.org/10.3847/1538-4357/ac4bbc)
- Thoul, A. A., Bahcall, J. N., & Loeb, A. 1994, *ApJ*, 421, 828, doi: [10.1086/173695](https://doi.org/10.1086/173695)
- Torres, G., Andersen, J., & Giménez, A. 2010, *A&A Rv*, 18, 67, doi: [10.1007/s00159-009-0025-1](https://doi.org/10.1007/s00159-009-0025-1)
- Tripathi, B., Nandy, D., & Banerjee, S. 2021, *MNRAS*, 506, L50, doi: [10.1093/mnras/rlab035](https://doi.org/10.1093/mnras/rlab035)
- Valenti, J. A., & Fischer, D. A. 2005, *ApJS*, 159, 141, doi: [10.1086/430500](https://doi.org/10.1086/430500)
- van Saders, J. L., Ceillier, T., Metcalfe, T. S., et al. 2016, *Nature*, 529, 181, doi: [10.1038/nature16168](https://doi.org/10.1038/nature16168)
- van Saders, J. L., & Pinsonneault, M. H. 2013, *ApJ*, 776, 67, doi: [10.1088/0004-637X/776/2/67](https://doi.org/10.1088/0004-637X/776/2/67)
- van Saders, J. L., Pinsonneault, M. H., & Barbieri, M. 2019, *ApJ*, 872, 128, doi: [10.3847/1538-4357/aafafe](https://doi.org/10.3847/1538-4357/aafafe)
- Vidotto, A. A., Gregory, S. G., Jardine, M., et al. 2014, *MNRAS*, 441, 2361, doi: [10.1093/mnras/stu728](https://doi.org/10.1093/mnras/stu728)
- Weber, E. J., & Davis, Leverett, J. 1967, *ApJ*, 148, 217, doi: [10.1086/149138](https://doi.org/10.1086/149138)
- Wood, B. E., Müller, H.-R., Redfield, S., et al. 2021, *ApJ*, 915, 37, doi: [10.3847/1538-4357/abfda5](https://doi.org/10.3847/1538-4357/abfda5)